

THE IMPACT OF GAS BULK ROTATION ON THE LYMAN- α LINE

JUAN N. GARAVITO-CAMARGO¹, JAIME E. FORERO-ROMERO¹, MARK DIJKSTRA²

Submitted for publication in ApJ

ABSTRACT

We present results of radiative transfer calculations to measure the impact of gas bulk rotation on the morphology of the Lyman α emission line in distant galaxies. We model a galaxy as a sphere with a homogeneous mixture of dust and hydrogen at a constant temperature. These spheres have a solid-body rotation with maximum velocities in the range $0 - 300 \text{ km s}^{-1}$ and neutral hydrogen optical depths in the range $\tau_H = 10^5 - 10^7$. We also consider two kinds of spatial distribution for the radiation sources with respect to the sphere: central and homogeneous. Our main finding is that the line width and the intensity at the line's center increase with rotational velocity. For homogeneously distributed sources the line becomes single peaked at rotational velocities larger than the line width in the static case. Under the same conditions the escape fraction increases $\sim 30\%$. For radiation sources located off-center, the line morphology presents a range of single, double and triple peaks. We show how these results are useful to interpret recent spectroscopic results of distant $z \sim 2 - 3$ star forming galaxies.

Subject headings: galaxies: high-redshift, galaxies: star formation, line: formation

1. INTRODUCTION

The detection of strong Ly α emission lines has become an essential method in extra-galactic astronomy to find distant star-forming galaxies (Partridge & Peebles 1967; Rhoads et al. 2000; Gawiser et al. 2007; Koehler et al. 2007; Ouchi et al. 2008; Yamada et al. 2012; Schenker et al. 2012). The galaxies detected using this method receive the name of Ly α emitters (LAEs). A detailed examination of this galaxy population has diverse implications for galaxy formation, reionization and the large scale structure of the Universe. Attempts to fully exploit the physical information included in the Ly α line require an understanding of all the physical factors involved in shaping the line. Due to the resonant nature of this line, these physical factors notably include temperature, density and bulk velocity field of the neutral Hydrogen in the emitting galaxy and its surroundings.

A basic understanding of the quantitative behavior of the Ly α line has been reached through analytic studies in the case of a static configurations, such as uniform slabs (Harrington 1973; Neufeld 1990) and uniform spheres (Dijkstra et al. 2006). Analytic studies of configurations including some kind of bulk flow only include the case of a sphere with a Hubble like expansion flow (Loeb & Rybicki 1999).

A quantitative description of the Ly α line has been reached through Monte Carlo simulations (Auer 1968; Avery & House 1968; Adams 1972). In the last two decades these studies have become popular due to the availability of computing power. Early into the 21st century, the first studies focused on homogeneous and static media (Ahn et al. 2000, 2001; Zheng & Miralda-Escudé 2002); Later on, the effects of clumpy media (Hansen & Oh 2006) and expanding/contracting shell/spherical geometries started to be studied (Verhamme et al. 2006;

Dijkstra et al. 2006). Similar codes have applied these results to semi-analytic models of galaxy formation (Orsi et al. 2012) and results of large hydrodynamic simulations (Forero-Romero et al. 2011, 2012; Behrens & Niemeyer 2013). Recently, Monte Carlo codes have also been applied to the results of high resolution hydrodynamic simulations of individual galaxies (Laursen et al. 2009; Barnes et al. 2011; Verhamme et al. 2012; Yajima et al. 2012). Meanwhile, recent developments have been focused on the systematic study of clumpy outflows (Dijkstra & Kramer 2012) and anisotropic velocity configurations (Zheng & Wallace 2013).

The recent studies of galaxies in hydrodynamic simulations (Laursen et al. 2009; Barnes et al. 2011; Verhamme et al. 2012; Yajima et al. 2012) have all shown systematic variations in the Ly α line with the viewing angle. These variations are a complex superposition of anisotropic density configurations (i.e. edge-on vs. face-on view of a galaxy), the inflows observed by gas cooling and the outflows included in the supernova feedback process of the simulation. These bulk flows physically correspond to the circumgalactic and intergalactic medium (CGM and IGM). These effects are starting to be studied in simplified configurations that vary the density and wind characteristics (Zheng & Wallace 2013).

However, in all these efforts the effect of rotation, which is an ubiquitous feature in galaxies, has not been systematically studied. The processing of the Ly α photons in a rotating interstellar medium (ISM) must have some kind of impact in the Ly α line morphology.

Performing that study is the main goal of this paper. We investigate for the first time the impact of rotation on the morphology of the Ly α line. We focus on a simplified system: a spherical gas cloud with homogeneous density and solid body rotation, to study the line morphology and the escape fraction in the presence of dust. We base our work on two independent Monte Carlo based radiative transfer codes CLARA (Forero-Romero et al. 2011) and XX (Dijkstra & Kramer 2012).

¹ Departamento de Física, Universidad de los Andes, Cra. 1 No. 18A-10, Edificio Ip, Bogotá, Colombia

² Max Planck Institute for Astrophysics, Karl-Schwarzschild-Str. 1, 85741, Garching, Germany

This paper is structured as follows: In §2 we present the implementation of bulk rotation into the Monte Carlo codes, paying special attention to coordinate definitions. We also present a short review of how the Ly α radiative transfer codes work and list the different physical parameters in the simulated grid of models. In the next §3 we present the results of the simulations, with special detail to quantities in the line that show a clear evolution as a function of the sphere rotational velocity. In §4 we discuss the implications of our results in the interpretation of LAEs observations. In the last section we present our conclusions.

In this paper we express a photon's frequency in terms of the dimensionless variable $x \equiv (\nu - \nu_a)/\Delta\nu_\alpha$, where $\nu_\alpha = 2.46 \times 10^{15}$ Hz is the Ly α resonance frequency, $\Delta\nu_\alpha \equiv \nu_\alpha \sqrt{2kT/m_p c^2} \equiv \nu_\alpha v_{th}/c$ is the Doppler broadening of the line which depends on the neutral gas temperature T scattering the radiation or equivalently the thermal velocity v_{th} of the atoms. For the temperature $T = 10^4$ K used in our radiative transfer calculations the thermal velocity is $v_{th} = 12.8$ km s $^{-1}$.

2. MODELS OF BULK GAS ROTATION

Describing the kinematics of gas rotation in all generality is a complex task, specially at high redshift where there is still missing a thorough observational account of rotation in galaxies beyond $z > 1.0$. Even at low red-shifts there is a great variation in the shape of the rotation curve as observed in HI emission as a function of the distance to the galaxy center. However there are two recurrent features. First, in the central galactic region the velocity increases proportional to the radius, following a solid rotation behavior. Second, beyond a certain radius the rotation curve tends to flatten.

An ab-initio description of realistic rotation curves in simulations depends on having access to the dynamic evolution of all mass components in the galaxy: stars, gas and dark matter. Such level of realism is extremely complex to achieve, specially if one wants to get a systematic description based on statistics of simulated objects.

Following the tradition of studies of Ly α emitting systems, we implement a model with simplified geometry. We assume that the gas is homogeneously distributed in a sphere that rotates as a solid body with constant angular velocity. This simple model will contain only one free parameter: the linear velocity at the sphere's surface, V_{max} .

2.1. Detailed Implementation of Rotation

In the Monte Carlo code we define a Cartesian coordinate system to describe the position of each photon. The origin of this system coincides with the center of the sphere and the rotation axis is defined to be z -axis. With this choice, the components of the gas bulk velocity field, $\vec{v} = v_x \hat{i} + v_y \hat{j} + v_z \hat{k}$, can be written as

$$v_x = -\frac{y}{R} V_{max}, \quad (1)$$

$$v_y = \frac{x}{R} V_{max}, \quad (2)$$

$$v_z = 0, \quad (3)$$

where R is the radius of the sphere and V_{max} is the linear velocity at the sphere's surface. The minus/plus sign in

the x/y -component of the velocity indicates the direction of rotation. In this case we take the angular velocity in the same direction as the \hat{k} unit vector. With these definitions we can write the angular velocity as $\omega = V_{max}/R$.

For each photon in the simulation we have its initial position inside the sphere, direction of propagation \hat{k}_{in} and reduced frequency x_{in} . The photon's propagation stops once they cross the surface of the sphere. At this point we store the position, the outgoing direction of propagation \hat{k}_{out} and the reduced frequency x_{out} . We define the angle Θ by $\cos \Theta = \hat{k} \cdot \hat{k}_{out}$, that is the polar angle of the outgoing photon with respect to the z axis. Following Zheng & Wallace (2013) we make the study of the anisotropic emission in terms of this angle..

2.2. Brief Description of the Radiative Transfer Codes

Here we briefly describe the relevant points for the two radiative transfer codes we have used. For a detailed description we refer the reader to the original papers Forero-Romero et al. (2011); Dijkstra & Kramer (2012).

The codes follow the individual scatterings of Ly α photons as it travels through a 3D distribution of neutral Hydrogen. At each scattering the frequency of the photon (in the laboratory frame) and its direction of propagation change. This change in frequency is due to the peculiar velocities of the Hydrogen atom that absorbed and reemitted the photon. If dust is present, the photon can interact either with a Hydrogen atom or dust grain. In the case of a dust interaction the photon can be either absorbed or scattered, this probability is encoded in the dust albedo, A , which we chose to be 1/2. In order to obtain accurate values for the escape fraction of photons in the presence of dust, we do not use any accelerating mechanism in the radiative transfer. Once the photons escape the gas distribution we store their direction at their direction of propagation and frequency at their last scattering.

The photons are thus emitted in some region of the gas distribution and follow a random walk in space and frequency until they escape the gas distribution or are absorbed by a dust grain. The initialization process for the Ly α photons has to specify its position, frequency and direction of propagation. In our case we select the initial frequency to be exactly the Ly α restframe frequency ($x = 0$) and the direction of propagation to be random following an flat probability distribution over the sphere.

The gas is completely defined by its geometry (i.e. sphere or slab), temperature T , Hydrogen optical depth τ_H , dust optical depth τ_a and the bulk velocity field \vec{v} . Here we treat the gas as homogeneous in density (τ_H , τ_a) and temperature.

2.3. Grid of Simulated Galaxies

In the Monte Carlo calculations we follow the propagation of $N_\gamma = 10^5$ numerical photons through different spherical galaxies. For each galaxy we vary at least one of the following parameters: the maximum rotational velocity V_{max} , the hydrogen optical depth τ_H , the dust optical depth τ_a and the initial distribution of photons with respect to the gas. There are 60 models initial combining all variations of the input parameters. Table 1 summarizes the models.

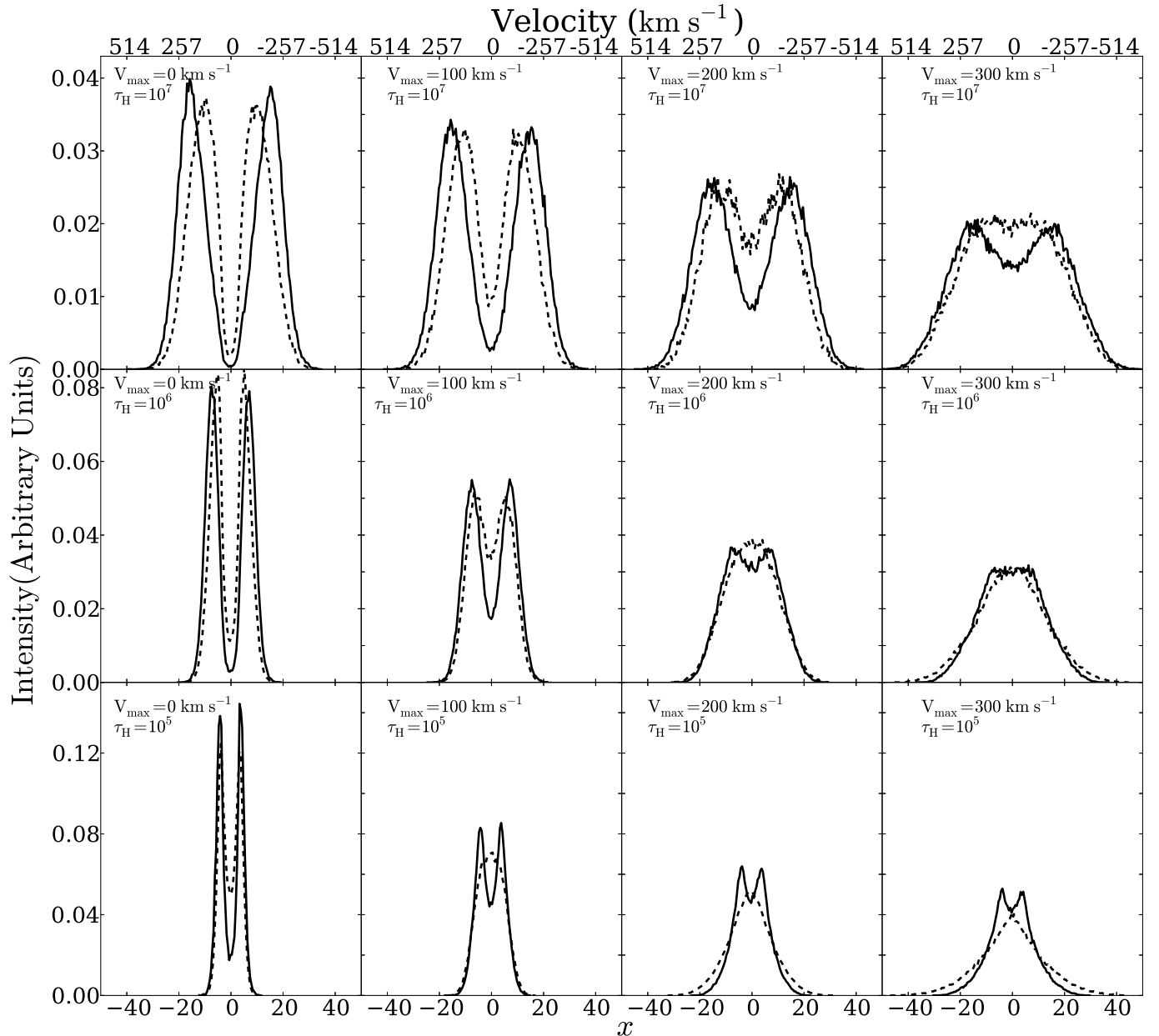


FIG. 1.— Shape of the Ly α line for different velocities rotational velocities for spherical distributions in all the models. The continous (dashed) line represents the central (homogeneous) source distributions.

Additionally, we have used two independently developed Monte Carlo codes (Forero-Romero et al. 2011; Dijkstra & Kramer 2012) to perform the calculations of the non-dusty models. The results we report are robust in the sense that they are obtained by both codes.

3. RESULTS

The central result of this paper is summarized in Figure 1. It shows the evident impact of rotation on the morphology of the emergent Ly α line. The panel focus on the results for all of our symmetric models $\tau_H = (10^6, 10^6, 10^5)$, showing that the influence of rotation is present both when the photons are either homogeneously or centrally initialized over the gas volume.

In the next subsections we characterize the line morphology by the full width at half maximum (FWHM) and

Physical Parameter (units)	Symbol	Values
Velocity (km s^{-1})	V_{max}	0, 50, 100, 200, 300
Hydrogen Optical Depth	τ_H	$10^5, 10^6, 10^7$
Dust Optical Depth	τ_a	0,1
Photons Distributions		Central, Homogeneous

TABLE 1

LIST OF THE PHYSICAL PARAMETERS THAT DEFINE THE SPHERICAL MODELS SIMULATED IN OUR MONTE CARLO CALCULATIONS. FOR EACH PARAMETER WE VARY THE VALUES IN THE RANGE LISTED IN THE LAST COLUMN. TAKING INTO ACCOUNT ALL THE POSSIBLE COMBINATIONS WE END UP WITH 60 DIFFERENT MODELS.

the location of the peak maxima. In order to interpret the morphological changes in the line we also report the median number of scatter for each Ly α photon in the simulation. For the models where dust is included we

measure the escape fraction as a function of rotational velocity. Finally, we make an estimate of the anisotropic emission of the models in comparison with static spheres.

3.1. Line width and peak maxima

There are three clear effects on the line's morphology as the rotational velocity increases. First, the line broadens; second, the double peaks reduce their intensity; and third, the intensity at the line center rises. The two last effects give the impression that the double peaks are merged into one at high rotational velocities, a result that is evident for the homogeneously distributed sources as shown in the dashed lines of Figure 1.

We use the full width at half maximum (FWHM) to quantify the line broadening. Figure 2 shows how the FWHM increases with rotational velocity both for the central and homogeneous source distributions. We parameterize the dependency of the linewidth as

$$\text{FWHM}^2 = \text{FWHM}_0^2 + V_{\text{max}}^2/\lambda^2, \quad (4)$$

where FWHM_0 is the velocity width in the static case and λ is a positive scalar to be determined as a fit to the data. With this test we want to know to what extent the new velocity width can be expressed as a quadratic sum of the two relevant velocities in the problem. We fit simultaneously all the points corresponding to central and homogeneous models to find $\lambda_c = 3.9 \pm 3.17 \times 10^{-17}$ and $\lambda_h = 1.9 \pm 3.07 \times 10^{-10}$ respectively. **EL ERROR ES de 10^{-17} ???**

In order to quantify the transition to a single peak we measure the position for the peak maxima as a function of the rotational velocity. Our results are presented in Figure 3 where it is clear that for central sources there are always two peaks with fixed positions as the rotational velocity changes. However, in the case of homogeneously emitted sources the maxima position remain close to constant until some velocity threshold the line becomes single peaked with $x_m = 0 \text{ km s}^{-1}$. By inspection we find that in all cases the transition has occurred when the rotational velocity is larger than half width.

One possible explanation for the emergence of the single peak in the homogeneous source systems is that some photons close to the surface (a sort of photosphere) can escape with a low number of scatterings, allowing them to stay close to the line's center. Increasing the rotational velocity V_{max} reduces the optical depth making the photosphere region effectively larger, increasing the number of photons escaping close to the line's center.

However, for the central emission the transition to a single peak is never completed in the range of explored parameters. The absence of a single peak phase could be partially explained by the absence of a photosphere, in this case the average number of scatterings to escape should remain close to constant as the rotational velocity increases. The rise in intensity at the line's center could instead mean that the scattering in a medium with bulk motion are inefficient in driving photons outside that frequency region.

In order to explore our interpretation for these two scenarios we now quantify the effect of rotation on the number of scatterings.

3.2. Average Number of Scatterings

The number of scatterings affects the escape frequency of a Ly α photon. In static cases, a large value of the optical depth correlates with a high number of scatterings, increasing the probability of finding a Ly α photon far from the line's center. As a result the peak maxima shifts from the center as the amount of neutral hydrogen increases. This can be precisely quantified in the static slab with central sources where the maxima position are related to the optical depth and the temperature as $x_m = \pm 1.066(a\tau_H)^{1/3}$ (Harrington 1973). In the same model the average number of scatterings depends only on the optical depth $\langle N_{\text{scatt}} \rangle = 1.612\tau_H$ (Adams 1972; Harrington 1973), in the case of homogeneously distributed sources $\langle N_{\text{scatt}} \rangle = 1.16\tau_H$ (Harrington 1973).

In Figure 4 we show the average number of scatterings $\langle N_{\text{scatt}} \rangle$ as a function of the rotational velocity V_{max} . For the central source distribution the average number of scatterings $\langle N_{\text{scatt}} \rangle$ changes less than 0.5% for different velocities. In this set-up the number of scatterings is proportional to the optical depth, with $\langle N_{\text{scatt}} \rangle = (1.50, 1.00, 0.92)\tau_H$ for optical depth values of $\tau_H = (10^5, 10^6, 10^7)$, respectively.

From Figure 4 is also clear that for the homogeneous distribution there is a clear decrease of $\langle N_{\text{scatt}} \rangle$ as the V_{max} increases. For instance, for $\tau_H = 10^5$ the average number of scatterings decreases by 61% at $V_{\text{max}} = 300 \text{ km s}^{-1}$ in comparison to the static case.

In this case we find that for a static sphere $\langle N_{\text{scatt}} \rangle = (0.99, 0.59, 0.51)\tau_H$, this represents factors of (0.66, 0.59, 0.55) lower than the centrally emitted photons. In contrast the analytic solution for the homogeneous slab gives 0.72 times less scatterings in the homogeneous case than in the central one.

In order to gain a deeper understanding of these results and explain the results for the maxima in the line morphology we make 2D histograms for the number of scatterings as a function of the outgoing dimensionless frequency x . In Figure 5 we show such histograms in the case $\tau_H = 10^5$ for the static case and $V_{\text{max}} = 300 \text{ km s}^{-1}$. The upper (lower) panels show the results for the homogeneous (central) source distribution. The color scale is logarithmic in the number of photons at a certain value $x-N_{\text{scatt}}$.

The top right panel of Figure 5 (homogeneous sources, high rotational velocity) supports our hypothesis about the photo-sphere in the homogeneous distribution. In this case most of the photons that left with $x \sim 0$ have escaped with less than 10 scatterings. This also explains the decrease in the average number of scatterings observed in Figure 4.

However, for a central distribution the situation is quite different (lower panels). In this case the number of scatterings remains high, in the order of the optical depth, but the two peaks do get closer to each other. Here the most probable physical picture is that each scattering, due to the bulk velocity of the gas, is inefficient in driving the photon outside the line center.

3.3. Dusty Clouds: Escape Fraction

In the case of dusty clouds, all changes in the average number of scatterings presented in the previous subsection have a direct bearing on the escape fraction. From the results we have just obtained we can predict that

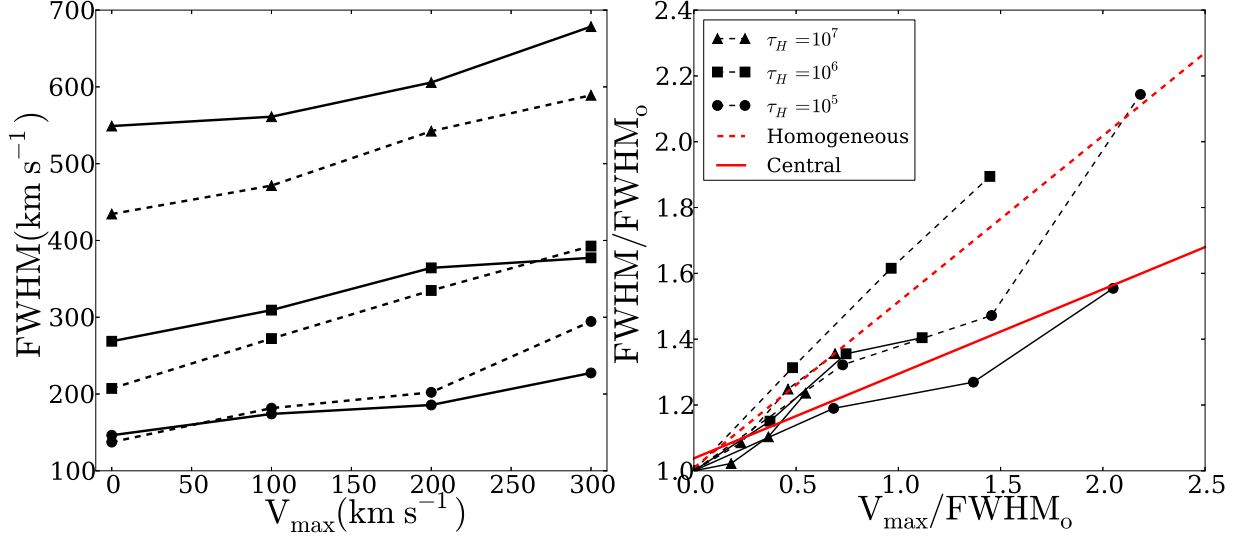


FIG. 2.— FWHM for the non-dusty models as a function of rotational velocity V_{\max} . The left panel shows the results in velocity units while the right panel normalizes the data by the FWHM in the static case. Continuous (dashed) lines correspond to central (homogeneous) source distributions. The straight lines represent the fit to the data using the expression in Eq. (4).

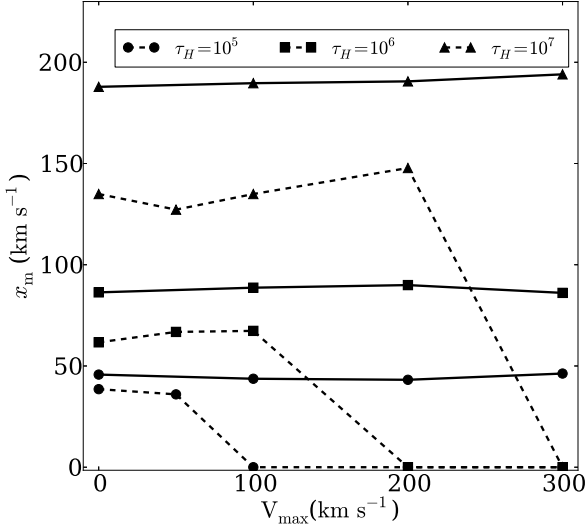


FIG. 3.— Position of the peak maxima as a function of rotational velocity V_{\max} . Continuous (dashed) lines correspond to central (homogeneous) source distributions. A value of $x_{\max} = 0$ indicates that line becomes single peaked.

Sources	τ_H	V_{\max} (km s ⁻¹)				
		0	50	100	200	300
Homogeneous	10 ⁵	0.263	0.266	0.309	0.357	0.370
	10 ⁶	0.289	0.289	0.309	0.360	0.393
	10 ⁷	0.227	0.229	0.231	0.254	0.281
Central	10 ⁵	0.096	0.097	0.096	0.096	0.096
	10 ⁶	0.066	0.066	0.066	0.066	0.066
	10 ⁷	0.015	0.016	0.016	0.016	0.015

TABLE 2
ESCAPE FRACTION VALUES FOR ALL DUSTY MODELS.

for central source distributions the escape fraction will barely change, while larger effects should be expected for homogeneously distributed sources.

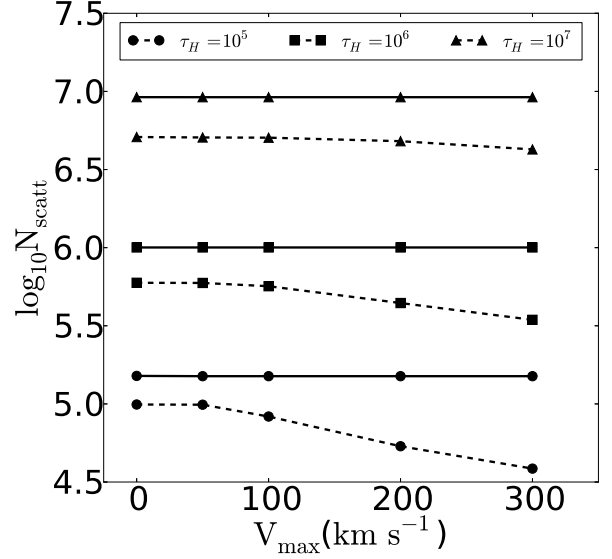


FIG. 4.— Logarithm of the average number of scatterings as function of rotational velocity. Continuous (dashed) lines represent an central (homogeneous) distribution of sources.

Figure 6 confirm these expectations. It shows the escape fraction as a function of the rotational velocity. The curves for the central source distribution stay flat, while for the homogeneous case there is a clear rise with rotational velocity. Rotation has a higher relative impact in the models with low optical depth. For instance, in models with $\tau_H = 10^5$, the static escape fraction is 0.26 and increases to 0.37 for $V_{\max} = 300$ km s⁻¹. Table 2 lists all the values for the escape fraction.

In the right panel of Figure 6 we put these results in the context of the analytic solution for the infinite slab (Neufeld 1990). In Neufeld's set-up the analytic solution depends uniquely on the product $(a\tau_H)^{1/3}\tau_a$, an approximation that is valid only in the limit $a\tau_H \gg 1$. The dashed lines in the right panel of Figure 6 show the results for the different rotational velocities. First of all

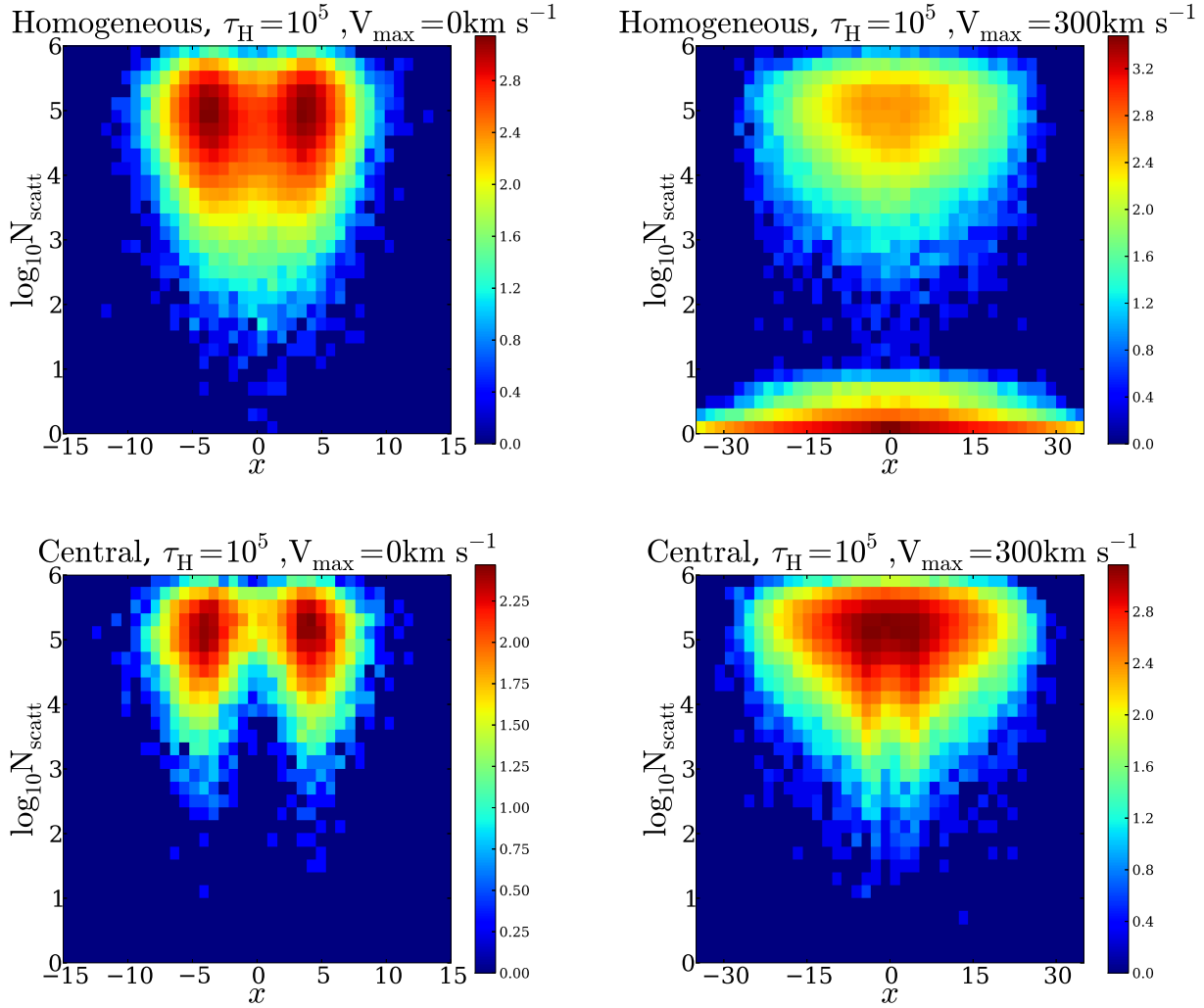


FIG. 5.— 2D histogram of N_{scatt} vs x . The upper (lower) panels show the homogeneous (central) source distribution. Left corresponds to the static case and right $V_{\text{max}} = 300 \text{ km s}^{-1}$. The color scale is logarithmic on the number of photons with given values of N_{scatt} and x .

we note that the escape fraction does not increase from $\tau_H = 10^5$ to $\tau_H = 10^6$, a fact that is explained since there is a transition from an opaque to an extremely opaque medium which affect affects how Ly α photons escape from the medium: single flight vs. single excursion. **Que quiere decir eso de single flight y single excursion, porque explica eso la fraccion de escape?**

3.4. Anisotropy and off-centered emission

Rotation breaks the spherical symmetry of the static model and introduces the rotation axis as a preferred direction. This motivates us to study the anisotropy of the outgoing photons. In order to study possible deviations with respect to an isotropic flux we follow Zheng & Wallace (2013) to estimate the flux as a function of the angle Θ formed by the outgoing photons and the observer. Figure 7 presents a geometric scheme to clarify the definition of all relevant directions in the problem.

An estimator for the anisotropy is represented by

$$F(\mu) = \frac{2\Delta N}{N\Delta\mu}, \quad (5)$$

where $\mu = \cos\Theta$, N is the total number of outgoing photons, ΔN is the number of photons in an angular bin $\Delta\Theta$. This definition satisfies the condition $\int_{-1}^1 F(\mu) d\mu/2 = 1$. With this definitions, the isotropic emission is characterized by a flat $F(\mu)$ distribution.

Figure 7 presents the results for the $F(\mu)$ distribution for an sphere with $\tau_H = 10^7$ and $V_{\text{max}} = 200 \text{ km s}^{-1}$. The dashed and dotted lines represent the homogeneous and central source distribution, respectively. This shows that the the anisotropy induced by rotation is at the 3% level. We performed the same test with all the models and find that the variation in μ does not depend on the rotational velocity; however, high optical depth values can increase the variation of μ up to a 15%.

We also explore a different source of anisotropy by studying the effect of radiation sources located in off-centered spheres with respect to the gas distribution. Figure 7 shows the two spherical regions we define to test for this effect. Each has a radius of $0.5R$, where R is the radius of the gaseous sphere. With an observer

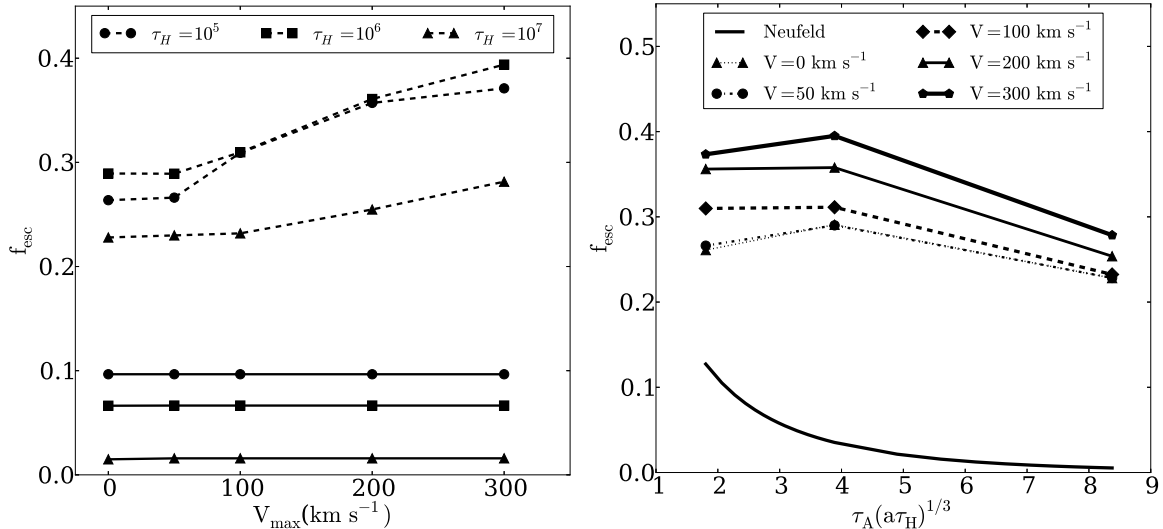


FIG. 6.— Effects of rotation on the escape fraction. Left panel. Escape fraction as a function of rotational velocity. All these models have $\tau_a = 1$. The continuous (dashed) lines correspond to central (homogeneous) models. Right panel. Escape fraction as a function of the product $(a\tau_H)^{1/3}\tau_a$. The analytic solution for the infinite slab is shown as a continuous line. Different lines correspond to different rotational velocities.

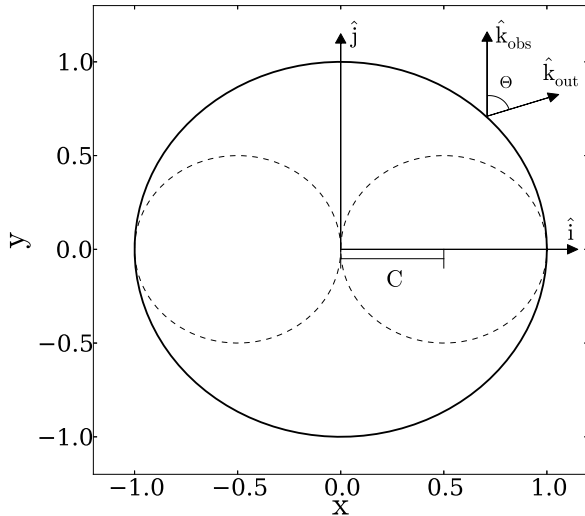


FIG. 7.— Schematic representation of the geometry for the off-center emission. The large circle represents the gas distribution and the two smaller circles the off-centered $\text{Ly}\alpha$ emitting regions. The angular velocity vector lies along \hat{k} direction towards the reader. The vector \hat{k}_{out} represents the outgoing direction of an escaping $\text{Ly}\alpha$ photon and the observer is placed along the \hat{j} direction. The distribution of Θ angles is used to study potential emission anisotropies.

located along the \hat{j} direction, we pick two possible positions to center the spheres along the \hat{k} axis: $\pm C\hat{k}$. In this configuration the emitting sphere centered on $+C\hat{k}$ moves away from the observer and the sphere centered on $-C\hat{j}$ moves towards the observer.

In this case the μ distribution is not homogeneous as shown in Figure 8. The off-center emission shows a variation of flux at the levels of 10% – 28% in intensity with the angle Θ . In general models with a larger τ_H present a higher variation in the flux. This variation implies that that the line is more intense in the plane perpendicular to the rotation axis.

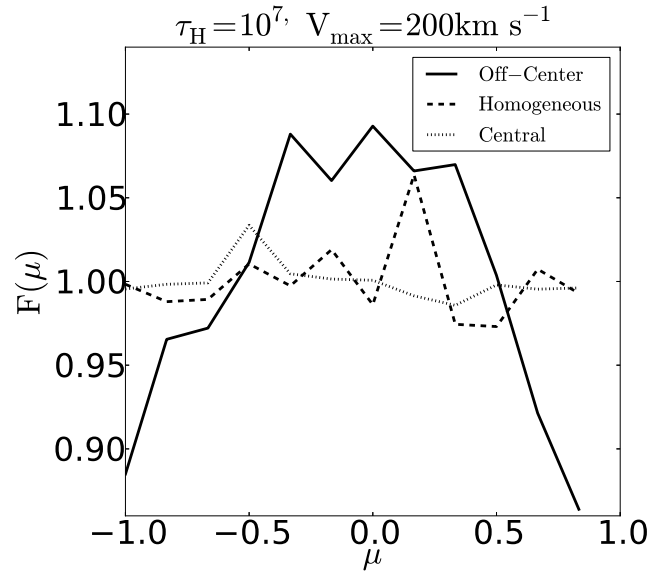


FIG. 8.— Histogram of $\mu \equiv \cos \Theta$ for the central (dotted), homogeneous (dashed) and off-center (solid line) distributions. Deviations from a flat distribution signal the presence of spatial emission anisotropies.

We also explore the effects of off-centered emission in the line morphology. Figure 9 shows the spectra for the two off-centered emitting spheres located at $C = \pm 0.5R$. In this case we only use photons that have outgoing directions aligned with the observer i.e. $0.9 < |\mu| < 1.0$. We do not find any strong asymmetry in the line morphology.

However, we find some cases where there is a possible signature of three peaks. This is only present in some models ($\tau = 10^6, V = 100 \text{ km s}^{-1}$ and $\tau = 10^7, V = 300 \text{ km s}^{-1}$) and could be the result of two competing effects: the rise in the line's center as the photons in the photosphere escape in a single excursion and the broadening in the two peaks as the photons closer from the center have to scatter to escape. We examine in greater

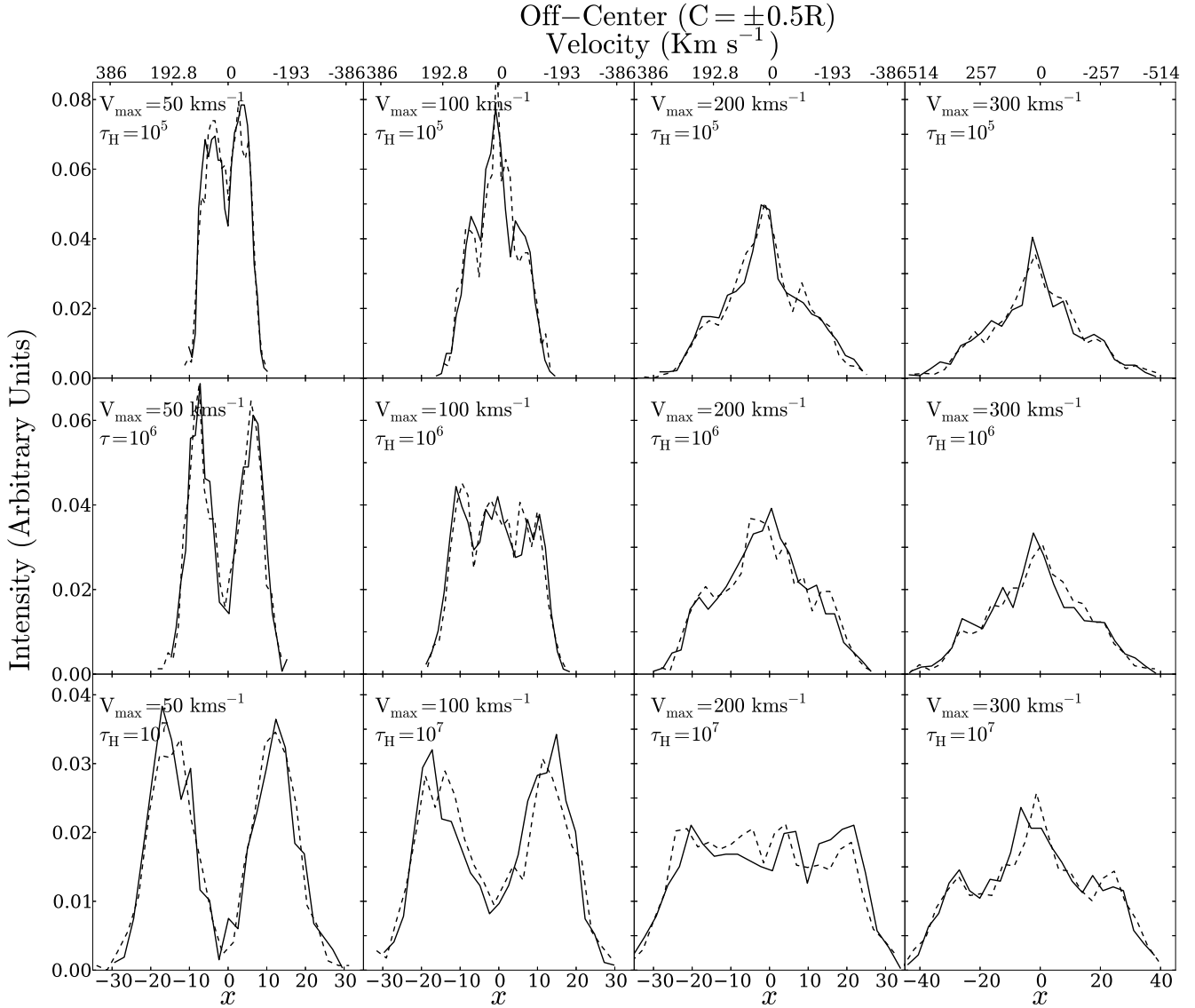


FIG. 9.— Ly α profiles for the off-centered emission. Dashed/solid lines represents spheres centered at $-0.5R$ / $+0.5R$ respectively.

detail these cases in the next sub-section.

3.5. Triple Peaked Profiles

The off-centered cases with hints of triple peaked emission motivate us to explore this in more detail. The first condition is to increase the number of photons in the radiative transfer calculation. In the line profiles presented in the previous subsection, only $\sim 10^4$ photons have the geometric conditions to build the line profile. We run a few models with $N_\gamma = 10^6$ in order to improve the statistics and explore smaller radii for the off-centered spheres.

We re-simulate four models that presented some signs of triple peaked profiles: $V_{\max} = 50 \text{ km s}^{-1}$, $\tau_H = 10^5$; $V_{\max} = 100 \text{ km s}^{-1}$, $\tau_H = 10^6$; $V_{\max} = 150 \text{ km s}^{-1}$, $\tau_H = 10^6$; and $V_{\max} = 200 \text{ km s}^{-1}$, $\tau_H = 10^7$. We select the photons that were emitted within spheres of radius $0.25R$ centered at $C = (0.25R, 0.5R, 0.75R)$, following the same geometry presented in Figure 7.

Figure 10 summarizes the results for all these mod-

els. In all cases the stronger triple peaked signatures is presented by the emitting spheres close centered at $0.75R$ close to the surface. Emitting spheres closer to the center do not show clear signatures for a triple peaked emission.

Furthermore, taking into account all the models that do not even present hints for a triple peaked emission it would seem that the rotational velocity and optical depth must balance each other in order to show this feature. Namely, if the rotational velocity is close to half the FWHM of the line, the triple peaks are more likely to occur. This is the same threshold that in the case of centered emission marks the difference between double and single peaked lines.

Are these features observable with current instrumental capabilities? As an order of magnitude estimate we can consider that the width of each one of the triple peaks is close to $1/3$ of the FWHM of the line at a given V_{\max} . For the cases we have studied in this subsection those values would be close to 50 km s^{-1} , 100 km s^{-1} and 200 km s^{-1} for optical depths of 10^5 , 10^6 , and 10^7 respec-

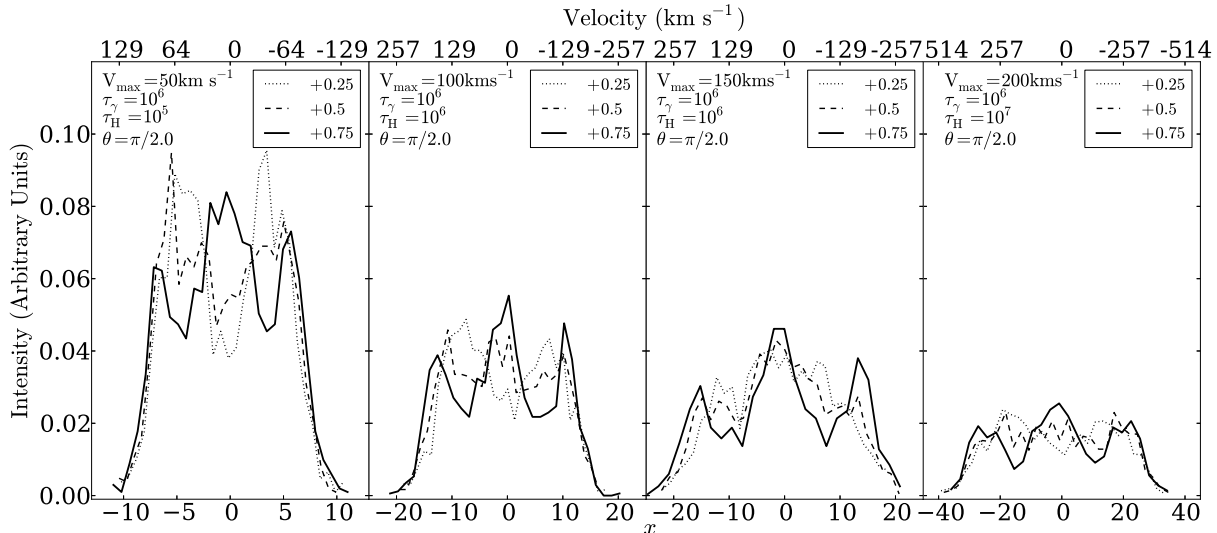


FIG. 10.— Triple peaked profiles for three different off-center positions $C = 0.25R$ (dotted line), $C = 0.5R$ (dashed line) & $C = 0.75R$ (solid line) and for different rotational velocities.

tively. At a redshift of $z \sim 2-3$ each one of these widths is multiplied by factors of $z+1 \sim 3-4$. Considering a nominal value for the resolution of $\Delta v = 200 \text{ km s}^{-1}$ for a Near-IR spectrograph capable of observing those galaxies (Kulas et al. 2012), we find that only the case of triple peaked emission for the most massive object $\tau_H, 10^7$, $V_{\text{max}} = 200 \text{ km s}^{-1}$ would have a chance to be spectrally resolved.

4. DISCUSSION

Gas bulk rotation has a noticeable effect on the morphology of the $\text{Ly}\alpha$ line. In this section we discuss the implications of these findings for the interpretation of available observational data. Our discussion focuses on the qualitative aspects of diverse morphological features observed by Kulas et al. (2012) and Yamada et al. (2012).

We follow a classification of $\text{Ly}\alpha$ profiles made by Kulas et al. (2012). They presented observational results for star forming galaxies at $z = 2-3$ with multiple peaks in their $\text{Ly}\alpha$ emission. They classified the observed lines into five groups. In Group I the red peak is stronger than the blue, while in Group II the blue peak is stronger, in both cases the peaks are symmetrically located around the line center. In Group III the blue peak also dominates but there is an overall redward shift of the zero point. Group IV presents two similar peaks symmetrically located around the zero point and Group V galaxies show three peaks.

The asymmetries in Groups I, II and III cannot be explained by rotation. However, some galaxies in those groups have a high flux between the two peaks; an effect that can be induced by rotation. The same argument applies to galaxies in the group IV in which the flux in between of the two peaks is high ($\geq 70\%$ of the intensity in the highest peak). Finally, the triple peaked lines in Galaxies in Group V can be easily reproduced by rotation with off-centered emission given the right amount of asymmetry between the emitting region and neutral hydrogen distribution.

Another relevant sample of observations was presented by Yamada et al. (2012) for 91 LAEs at $z = 3.1$. They

find that $\sim 33\%$ of the galaxies present a single peak profile. Some of the peaks have a strong symmetry, while others do not. The symmetric single peaked profile can be explained by rotation effects, while the asymmetric cases naturally arise in outflow/inflow models (Verhamme et al. 2008; Dijkstra et al. 2006). Among the 91 LAEs, 8 reveal triple peaked profiles with a central peak and two smaller peaks at the redder and bluer side, a feature that is present in our off-center emission models with rotation Figure 10.

The presence of single peaked profiles has been associated to inflow/outflow dynamics (?). In this paper we show that gas bulk rotation can also be considered as a probable origin for that behavior, provided that the observed single peak is highly symmetric. Similarly, in the case of double peaked lines with a high level of flux at the line center, rotation also deserves to be considered in the pool of possible bulk flows responsible for that feature, specially if the two peaks have similar intensities. The case of triple peaked lines is another clear feature of gas rotation under the additional condition of an off-centered emission.

5. CONCLUSIONS

This paper quantifies for the first time in the literature the effects of rotation in the morphology of the $\text{Ly}\alpha$ emission line in star forming galaxies. The results are based on the study of an homogeneous sphere of gas with solid body rotation. We explore a range of models by varying the rotational speed, hydrogen optical depth, dust optical depth and initial distribution of $\text{Ly}\alpha$ photons with respect to the gas density. As a cross-validation, we obtain our results from two independently developed Monte-Carlo radiative transfer codes.

Our main result is that rotation clearly impacts the $\text{Ly}\alpha$ line morphology. Double peaked lines can make transitions into single peaked lines as the rotational velocity increases. In the case of off-centered emission result into triple peaked lines for certain values of optical depth and rotational velocities.

Quantitatively the main results of our study are sum-

marized as follows.

- The line width increases with rotational velocity. The line with approximately following the functional for $\text{FWHM}^2 = \text{FWHM}_0^2 + (V_{\text{max}}/\lambda)^2$ where FWHM_0 indicates the line width for the static case. λ is a constat determined from the radiative transfer results it is $\lambda_c = 3.9 \pm$ and $\lambda_h = 1.9 \pm$ for the central and homogeneous source distribution, respectively.
- A single peaked line emerges for high rotational velocities in the case of homogeneously distributed sources. These cases occur when the rotational velocity is larger than $h\text{FWHM}_0$.
- For central sources we find that the number of scatterings does not significantly decrease with rotation. This is due to the fact that the vast majority of scatterings events are resonant, during which the mean free path is very short and the effect of gas bulk rotation is not enough to affect Ly α photons. In consequence, the escape fraction neither the position of the peaks depende on the rotational velocity. However, there is a flux increase with rotational velocity in the central parts of the line.
- For homogeneous sources we find that the changes in the line morphology are linked to the reduction in the average number of scatterings. In the second part of §3.1 we show that, as rotational velocity increases, a large fraction of photons escape with less than 10 scatterings. The avarage number of

scatterings decreases a 40% compared to the static case. The reduction in the number of scattering decreases the probability for a photon to move away from the line's center. This is also translated into an increase of the escape fraction by a factor of ~ 2 with respect to the static situation.

- The spatial anisotropies in the emission are always at a level below the 10% deviation from static models.
- For off-centered emission triple peaked profiles can emerge under two conditions: the emission occurs close to th sphere's surface and the rotational velocity is half the FWHM in the static case.

Comparing our results with recent observed LAEs we find that many morphological features such as high central line flux, single peak profiles and multi-peaked profiles could be explained by gas bulk rotation present in these LAEs.

ACKNOWLEDGEMENTS

JNGC acknowledges financial support from Universidad de los Andes.

JEFR acknowledges financial support from Vicerrectoria de Investigaciones at Universidad de los Andes through a FAPA grant.

We thank the International Summer School on AstroComputing 2012 organized by the University of California High-Performance AstroComputing Center (UC-HiPACC) for providing computational resources where some of the calculations were done.

REFERENCES

- Adams, T. F. 1972, *ApJ*, 174, 439
- Ahn, S.-H., Lee, H.-W., & Lee, H. M. 2000, *Journal of Korean Astronomical Society*, 33, 29
- . 2001, *ApJ*, 554, 604
- Auer, L. H. 1968, *ApJ*, 153, 783
- Avery, L. W., & House, L. L. 1968, *ApJ*, 152, 493
- Barnes, L. A., Haehnelt, M. G., Tescari, E., & Viel, M. 2011, *MNRAS*, 416, 1723
- Behrens, C., & Niemeyer, J. 2013, *A&A*, 556, A5
- Dijkstra, M., Haiman, Z., & Spaans, M. 2006, *ApJ*, 649, 14
- Dijkstra, M., & Kramer, R. 2012, *MNRAS*, 424, 1672
- Forero-Romero, J. E., Yepes, G., Gottlöber, S., Knollmann, S. R., Cuesta, A. J., & Prada, F. 2011, *MNRAS*, 415, 3666
- Forero-Romero, J. E., Yepes, G., Gottlöber, S., & Prada, F. 2012, *MNRAS*, 419, 952
- Gawiser, E., Francke, H., Lai, K., Schawinski, K., Gronwall, C., Ciardullo, R., Quadri, R., Orsi, A., Barrientos, L. F., Blanc, G. A., Fazio, G., & Feldmeier, J. J. 2007, *ApJ*, 671, 278
- Hansen, M., & Oh, S. P. 2006, *MNRAS*, 367, 979
- Harrington, J. P. 1973, *MNRAS*, 162, 43
- Koehler, R. S., Schuecker, P., & Gebhardt, K. 2007, *A&A*, 462, 7
- Kulas, K. R., Shapley, A. E., Kollmeier, J. A., Zheng, Z., Steidel, C. C., & Hainline, K. N. 2012, *ApJ*, 745, 33
- Laursen, P., Sommer-Larsen, J., & Andersen, A. C. 2009, *ApJ*, 704, 1640
- Loeb, A., & Rybicki, G. B. 1999, *ApJ*, 524, 527
- Neufeld, D. A. 1990, *ApJ*, 350, 216
- Orsi, A., Lacey, C. G., & Baugh, C. M. 2012, *MNRAS*, 425, 87
- Ouchi, M., Shimasaku, K., Akiyama, M., Simpson, C., Saito, T., Ueda, Y., Furusawa, H., Sekiguchi, K., Yamada, T., Kodama, T., Kashikawa, N., Okamura, S., Iye, M., Takata, T., Yoshida, M., & Yoshida, M. 2008, *ApJS*, 176, 301
- Partridge, R. B., & Peebles, P. J. E. 1967, *ApJ*, 147, 868
- Rhoads, J. E., Malhotra, S., Dey, A., Stern, D., Spinrad, H., & Jannuzi, B. T. 2000, *ApJ*, 545, L85
- Schenker, M. A., Stark, D. P., Ellis, R. S., Robertson, B. E., Dunlop, J. S., McLure, R. J., Kneib, J.-P., & Richard, J. 2012, *ApJ*, 744, 179
- Verhamme, A., Dubois, Y., Blaizot, J., Garel, T., Bacon, R., Devriendt, J., Guiderdoni, B., & Slyz, A. 2012, *A&A*, 546, A111
- Verhamme, A., Schaerer, D., Atek, H., & Tapken, C. 2008, 111, 89
- Verhamme, A., Schaerer, D., & Maselli, A. 2006, *A&A*, 460, 397
- Yajima, H., Li, Y., Zhu, Q., Abel, T., Gronwall, C., & Ciardullo, R. 2012, *ApJ*, 754, 118
- Yamada, T., Nakamura, Y., Matsuda, Y., Hayashino, T., Yamauchi, R., Morimoto, N., Kousai, K., & Umemura, M. 2012, *AJ*, 143, 79
- Zheng, Z., & Miralda-Escudé, J. 2002, *ApJ*, 578, 33
- Zheng, Z., & Wallace, J. 2013, *ArXiv e-prints*